ADVANCED MATERIALS
www.advmat.de

Tailoring the Atomic-Local Environment of Carbon Nanotube Tips for Selective H_2O_2 Electrosynthesis at High Current Densities

Yongde Long, Jinguo Lin, Fenghui Ye, Wei Liu, Dan Wang, Qingqing Cheng, Rajib Paul, Daojian Cheng, Baoguang Mao, Riqing Yan, Linjie Zhao, Dong Liu, Feng Liu,* and Chuangang Hu**

The atomic-local environment of catalytically active sites plays an important role in tuning the activity of carbon-based metal-free electrocatalysts (C-MFECs). However, the rational regulation of the environment is always impeded by synthetic limitations and insufficient understanding of the formation mechanism of the catalytic sites. Herein, the possible cleavage mechanism of carbon nanotubes (CNTs) through the crossing points during ball-milling is proposed, resulting in abundant CNT tips that are more susceptible to be modified by heteroatoms, achieving precise modulation of the atomic environment at the tips. The obtained CNTs with N,S-rich tips (N,S-TCNTs) exhibit a wide potential window of 0.59 V along with H_2O_2 selectivity for over 90.0%. Even using air as the O_2 source, the flow cell system with N,S-TCNTs catalyst attains high H_2O_2 productivity up to 30.37 mol $g_{cat.}^{-1}$ h^{-1}@350 mA cm^{-2}, superior to most reported C-MFECs. From a practical point of view, a solid electrolyzer based on N,S-TCNTs is further employed to realize the in-situ continuous generation of pure H_2O_2 solution with high productivity (up to 4.35 mmol cm^{-2} h^{-1}@300 mA cm^{-2}; over 300 h). The CNTs with functionalized tips hold great promise for practical applications, even beyond H_2O_2 generation.

1. Introduction

Electrochemical synthesis of hydrogen peroxide (H_2O_2) is a promising alternative to the energy-demanding and waste-intensive anthraquinone cycling method.[1] However, the widespread application of electrochemical in situ generation of H_2O_2 is always hindered by the inferior activity and selectivity of the catalysts toward the two-electron oxygen reduction reaction (2e-ORR) pathway. The atomic-local environment (e.g., doping and defect engineering) of carbon-based metal-free electrocatalysts (C-MFECs) has been demonstrated to play a vital role in upgrading the catalytic activity and selectivity of 2e-ORR.[1b,2] A classic method is to improve the 2e-ORR performance of C-MFECs by introducing oxygen heteroatoms into the carbon skeleton.[1c,3] On this basis, additional types of heteroatoms have also been introduced to co-modify the atomic-local environment

Y. Long, F. Ye, D. Wang, D. Cheng, B. Mao, R. Yan, L. Zhao, D. Liu, C. Hu
State Key Laboratory of Organic–Inorganic Composites
College of Chemical Engineering
Beijing University of Chemical Technology
Beijing 100029, China
E-mail: bgmao@buct.edu.cn; chuangang.hu@mail.buct.edu.cn

J. Lin, F. Liu
State Key Laboratory of Nonlinear Mechanics
Institute of Mechanics
Chinese Academy of Sciences
Beijing 100190, China
E-mail: liufeng@imech.ac.cn

W. Liu
College of Materials Science and Engineering
Beijing University of Chemical Technology
Beijing 100029, China

Q. Cheng
Shanghai Advanced Research Institute
Chinese Academy of Sciences
Shanghai 201210, China

R. Paul
Advanced Materials and Liquid Crystal Institute
Kent State University
Kent, OH 44242, USA

The ORCID identification number(s) for the author(s) of this article can be found under https://doi.org/10.1002/adma.202303905

DOI: 10.1002/adma.202303905

of the active sites for further enhancing the 2e-ORR performance through the synergistic effect.[2b,4] Although most C-MFECs with oxygen modulations can enhance H_2O_2 selectivity along with increasing onset potentials, it requires high overpotential to deliver industrially relevant current density due to the high charge transfer resistivity caused by surface oxidation.[1b,3b,5] Therefore, developing an effective and facile method to tune C-MFECs for H_2O_2 generation with high activity and selectivity simultaneously at high current densities, is crucial for the practical application of in situ H_2O_2 electrosynthesis technologies.

Owing to the presence of abundant dangling bonds, the lattice edges of graphitic carbon materials may exhibit higher tunability than the basal plane,[6] which is expected to further optimize its electrocatalytic performance. For instance, various edge-functionalized graphene nanoplates (EFGnPs), such as edge-nitrogenated GnPs,[7] carboxylic acid functionalized GnPs,[8] edge-halogenated GnPs,[9] were prepared and demonstrated to be efficient C-MFECs toward four-electron-transfer ORR.[7,10] In addition, benefiting from the unique 1D structural morphology, hollow geometry, and ballistic carrier conduction, carbon nanotubes (CNTs) with relatively intact walls could effectively promote the mass transfer of reactants and products at high current density.[11] In this context, the construction of CNT-based C-MFECs with abundant functionalized tips but relatively intact walls may be expected to provide a possible scenario to simultaneously address the challenges of the activity for 2e-ORR and the requirement for electron conduction and mass transfer of reactants and products at industrial current densities. However, it remains a great challenge to precisely tune the atomic environments at CNT tips, ensuring the minimum effect on the walls to maintain high conductivity and maximize the tip density of CNTs to meet the demand for industrial current densities.

Herein, we demonstrated that the N, S co-modified atomic environment of CNT zigzag edge tips endows CNTs with superior 2e-ORR performance. First, we proposed a possible cleavage mechanism of CNTs during ball milling via molecular dynamics (MD) simulations and experimental data analysis, which preferentially occurs at the crossing region between entangled CNTs along with abundant zigzag edge tips. Moreover, based on adsorption free energy of key intermediate *OOH from density functional theory (DFT) calculations, the correlation of the geometric sites at the zigzag edges of tip-doped CNTs (TCNTs) with N and/or S doping was analyzed, predicting that the optimal active sites for 2e-ORR are the combined amino-*N* and thiophene-*S* with moderate distance. Then, gram-level TCNTs with N, S co-doped zigzag tips were fabricated by an optimized ball milling process. The typical catalyst endows enhanced H_2O_2 selectivity [94.5%@0.56 V vs reversible hydrogen electrode (RHE), all the potentials used in current work are with regard to RHE, if not indicated], wide potential window (PW) (H_2O_2 selectivity over 90.0% from 0.19 to 0.78 V), positive onset potential (0.78 V), and high H_2O_2 production rate (30.37 mol $g_{cat.}^{-1}$ h^{-1} at 350 mA cm^{-2}) in three-electrode setups. Even using natural air as the O_2 source, the cell voltage and Faraday efficiency (FE) of the equipped two-electrode flow cell (2E-FC) show almost no degradation after 200 hours of continuous operation. From an application point of view, the synthesis of pure H_2O_2 solution in air-based solid electrolyte cells (SEC) still achieved high FE (up to 95.1%@150 mA cm^{-2}) and H_2O_2 production rate (4.35 mmol cm^{-2} h^{-1} at a partial current of ≈233.2 mA cm^{-2}). This work provides promising C-MFECs for H_2O_2 production at high current density with great selectivity and presents a valuable strategy to fabricate optimal TCNTs for other critical electrochemical applications for energy conversion and storage beyond H_2O_2 generation.

2. Results and Discussion

2.1. Theoretical Investigation of Cleavage Mechanism and Tip Catalytic Site of CNTs

Compared with long CNTs, corresponding short CNTs have more tips for certain lengths, which are beneficial to increase potential active sites to improve electrocatalytic activity. To obtain short CNTs with abundant tip carbon edges, mechanical cutting is considered an efficient method.[12] Due to the large aspect ratio and Van der Waals force, CNTs usually tend to be entangled with each other, rather than isolated individual CNT.[13] In this case, the cleavage of CNTs is strongly related to the interaction among CNTs. In order to investigate the cleavage mechanism of CNTs more intuitively, we simplify the model to two entangled CNTs with their two ends pulling in opposite directions and using MD simulations to reveal the fracture evolution process of CNTs. Owing to the enhanced interaction between CNTs during ball milling, they gradually deform and eventually fracture from the high-stress concentration at the crossing regions (**Figure 1**a; Figure S1, Supporting Information).

After cleavage, the tip of CNTs exhibits jagged structures with abundant dangling bonds (Figure 1b). More importantly, the zoomed fracture region (CNT tip) shows that the majority of edges belong to zigzag type (Figure 1b). In addition, similar phenomena are also observed in other chiral CNTs (Figure S2, Supporting Information) and double-wall CNT (Figure S3, Supporting Information). In this context, doping heteroatom(s) on CNTs during their fracture may be a facile and efficient way to prepare heteroatom(s) doped CNTs. To clarify where the heteroatoms favor being doped in tip-rich CNTs during the cleavage process, the relative formation energy of several models of CNTs doped with heteroatoms (N or S) on the sidewall (basal plane) and tip (zigzag edge) were analyzed (Figure S4, Supporting Information). As shown in Figure 1c, the relative formation energy of edge models, especially eN-3 (pyrrolic-*N*), eN-4 (amino-*N*), and eS-3 (thiophene-*S*), is lower than those of basal plane models. Thus, heteroatoms are favor to be doped at the zigzag edges of CNTs to form TCNTs.

We then performed DFT calculations to disclose the potential 2e-ORR electrocatalytic performance of heteroatom-doped CNT tips with zigzag edges. Pyrrolic-*N*, amino-*N*, and thiophene-*S* with lower relative formation energy were also reported to be beneficial for 2e-ORR.[14] Thus, pure zigzag edges (pZE) and several heteroatom doping configurations at the zigzag edges, including pyrrolic-*N* (ZE_{NH}), amino-*N* (ZE_{NH2}), and thiophene-*S* (ZE_S) doped zigzag edges, were considered to investigate the 2e-ORR activities by first principle calculations (Figure S5a–d, Supporting Information). DFT calculations were performed to obtain the adsorption free energy of key intermediate *OOH (ΔG_{*OOH}),[1c] which was used as a descriptor to predict the 2e-ORR performance.[1b,15] Gibbs free energy (Figure 1d) and corresponding limiting potential (U_L) diagram (Figure 1e) suggest that

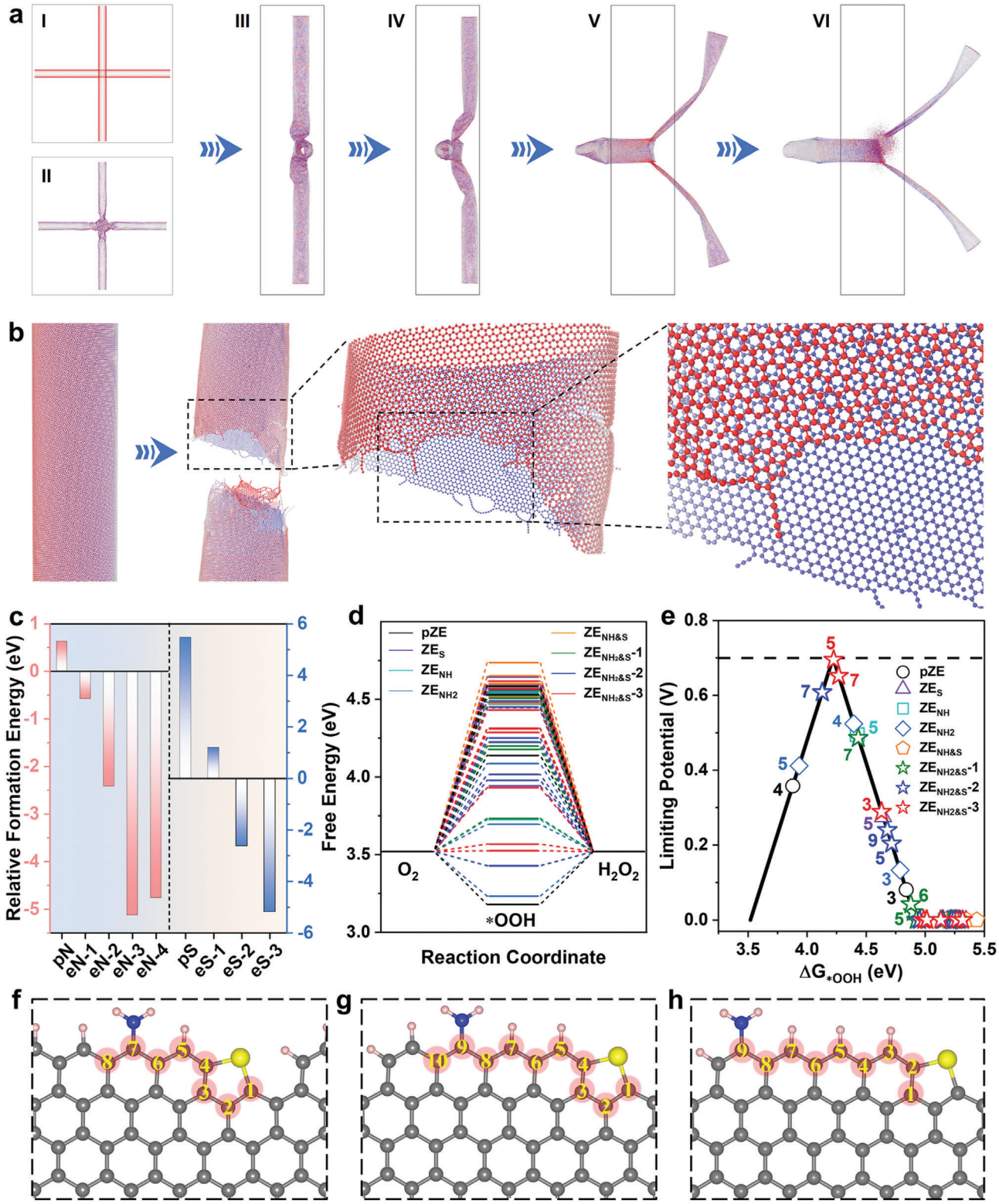

Figure 1. Cleavage mechanism and tip active sites of CNTs. a) Schematic diagram of initial (I), deformation (II–V), and fracture (VI) state on two entangled CNTs under stretching. I-II are a front view and III–VI are a side view. The darker the color, the higher the shear stress in II–VI. b) Configuration of (112, 28) CNT before and after fracture, and the enlarged tip morphology. c) The relative formation energy of several heteroatom-doped CNT sidewall (pN, pS) and tip (eN-1, eN-2, eN-3, eN-4, eS-1, eS-2, and eS-3) models. d) Gibbs free energy diagram along with the reaction steps on the zigzag edges. e) Calculated 2e-ORR related volcano plot, that is, U_L versus ΔG_{*OOH}. The configurations of f) $ZE_{NH2\&S}$-1, g) $ZE_{NH2\&S}$-2, and h) $ZE_{NH2\&S}$-3. Color code: carbon, gray; nitrogen, blue; sulfur, yellow; hydrogen, light pink.

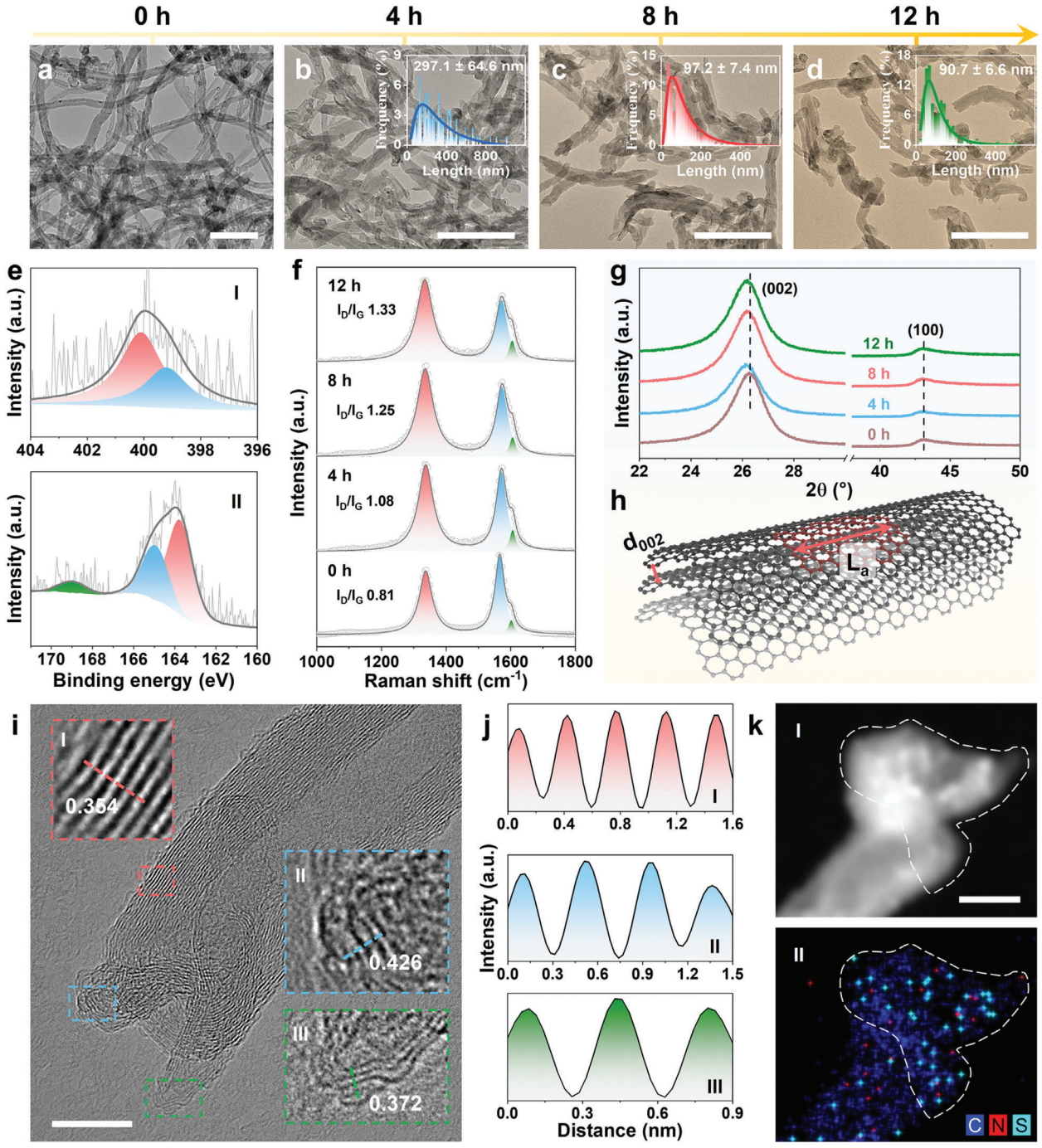

Figure 2. Synthesis and characterization of TCNTs. TEMs images and the length distribution (inserts) of a) pCNTs, b) N,S-TCNTs-4h, c) N,S-TCNTs-8h, and d) N,S-TCNTs-12h. Scale bar: 200 nm. e) HR-XPS spectra of (I) N 1s and (II) S 2p for N,S-TCNTs. f) Raman spectra and g) XRD patterns of pCNTs and TCNTs with different ball-milling times. h) Illustration of d_{002}, L_a in CNTs. i) HR-TEM image of N,S-TCNTs (scale bar: 10 nm). The insets are enlarged images of selected areas. j) Linear profiles obtained from the corresponding IFFT of corresponding selected areas. k) HADDF-STEM image (I, scale bar: 10 nm) and (II) corresponding EDS mapping of C, N, and S elements of N,S-TCNTs (the CNT tip is labeled in dash line circle).

the U_L of pZE (Figure S6, Supporting Information) and single heteroatom doped configurations (ZE_S, ZE_{NH}, ZE_{NH2}, Figures S7–S9, Supporting Information) are located on different sides of the volcano, indicating that the *OOH binding is either too strong (ZE_{NH}, ZE_S at left side) or too weak (ZE_{NH2} at right side). Thus, the single-component heteroatom doping is not beneficial to the efficient H_2O_2 generation, which intuitively calls for combining different functional groups to obtain a better 2e-ORR activity. However, compared to the separate pyrrolic-*N* and thiophene-*S*, the combination of them (Figure S5e, Supporting

Information) presents a much weaker *OOH binding and lower U_L (Figure 1e; Figure S10, Supporting Information). It is worth noting that the U_L of the fifth site in both ZE_S and ZE_{NH2} models is located at different sides close to the volcano (Figure 1e). Conceivably, the combination of amino-*N* and thiophene-*S* functional groups could introduce sites similar to the fifth sites, which may regulate the ΔG_{*OOH} to locate between them and make the U_L very close to the position of the volcano associated with the optimal 2e-ORR activity. To further verify this viewpoint, a combined model of amino-*N* and thiophene-*S* groups was chosen as a representative to reveal the synergistic effect for better 2e-ORR activity. Three configurations of amino-*N* and thiophene-*S* doped carbon edges with different distances between the functional groups were calculated ($ZE_{NH2\&S}$-1, $ZE_{NH2\&S}$-2, and $ZE_{NH2\&S}$-3, Figure 1f–h; Figure S5f-h, Supporting Information). As expected, the U_L of several sites in these configurations distribute between those of the fifth sites in ZE_{NH2} and ZE_S models, and three sites of them (especially the fifth and seventh sites in $ZE_{NH2\&S}$-3) are much closer to the volcano than others (Figure 1e; Figure S11, Supporting Information). Thus, the introduction of amino-*N* and thiophene-*S* simultaneously with moderate distance at the zigzag edges would promote the 2e-ORR. In short, DFT calculations reveal the synergistic effect of N and S dopants at the tips for boosting catalytic performance toward 2e-ORR.

2.2. Synthesis and Characterization of TCNTs

Guided by the above theoretical simulations, we attempted to prepare N and S co-doped TCNTs (N,S-TCNTs) by ball-milling the purified CNT (pCNTs, Figure S12, Supporting Information), which is a green approach with low-cost, and suitable for large-scale preparation.[8] The thus-obtained series of samples at different ball milling times (*x*) (named as N,S-TCNTs-*x*h; if not mentioned, "N,S-TCNTs" represents N,S-TCNTs-8h) were characterized by transmission electron microscope (TEM) (Figure 2a–d). As shown in **Figure 2**a and Figure S13a,b (Supporting Information), pristine CNTs are tangled with each other and with many cross joints. After ball milling, CNTs are shortened and keep the tubular structure with a large number of tips generated (Figure 2b–d; Figure S13c–h, Supporting Information). In addition, N,S-TCNTs show a much smaller contact angle than that of pCNTs, which ensure exposure to the electrolyte (Figure S14, Supporting Information). The length of those TCNTs fitted a lognormal distribution (insets in Figure 2b–d), and the mean length ($\bar{L}$) of TCNTs tended to be uniform with prolonging ball milling time within a certain time (Figure S15, Supporting Information),[12] indicating that the cleavage of CNTs is strongly related to the interaction among CNTs. However, when the ball milling time was increased to a longer time, like 48 h (CNTs-48h), the structure of CNTs is severely damaged (Figure S16, Supporting Information), possibly due to the short CNTs losing the entanglement characteristic of long CNTs. The fracture of CNTs suggests the cleavage of the "C—C" bond and the formation of numerous active carbon species (i.e., carbon radicals, carbocations, and carbanions.[3b,8,16]), which may be readily doped with heteroatom(s) during ball milling, making heteroatoms prone to be implanted at the tips of the formed CNTs.

Subsequently, the surface chemical configurations of heteroatoms were investigated by X-ray photoelectron spectroscopy (XPS, Figure S17a, Table S1, Supporting Information). The N 1s HR-XPS spectra can be deconvoluted into pyrrolic-*N* at ≈400.1 eV[7,17] and amino-*N* at ≈399.2 eV;[14c] and the S 2p HR-XPS peaks at ≈164.2 and 165.4 eV correspond to the $S_{3/2}$ and $S_{1/2}$ of thiophene-*S*, and an additional peak located at ≈169.0 eV should arise from oxidized sulfur[18] (Figure 2e; Figure S17b,c, Supporting Information), indicating the successful doping of N and S in the carbon framework of N,S-TCNT samples. Besides, the statistical elemental contents were also obtained from quantitative elemental analysis (EA), the N and S contents are increased with prolonging the ball milling time (Table S2, Supporting Information). In addition, the structure of the obtained-CNTs was further verified by Raman spectra (Figure 2f), in which the peaks centered at 1336 (D band), 1573 (G band), and 1606 cm^{-1} can be assigned to the disordered lattice points, the in-plane stretching vibration of sp^2-hybridized carbon atoms in ideal graphite lattices, and vibrations perpendicular to the CNT sidewalls,[19] respectively. With the extension of ball milling time from 4 h through 8 h to 12 h, the I_D/I_G (integral intensity ratio of D and G bands) values of TCNTs increased from 1.08 through 1.25 to 1.33, which are larger than that of pCNTs, most likely due to the ball milling process produced abundant tips with doping of heteroatoms.[7–9]

Furthermore, the X-ray diffraction (XRD) characteristic (002) peak of pCNTs is located at ≈26.3°,[1c] while that of TCNTs is slightly shifted lower to 26.2°, and the corresponding d-spacing (d_{002}) of TCNTs is little larger than that of pCNTs (Figure 2g, Table S3, Supporting Information), which may be attributed to the doping of N, S heteroatoms.[7–9] The average crystallite size along the basal plane (L_a) of graphitic lattice calculated from (100) diffraction peak according to the Scherrer equation, is used to evaluate the crystallite size along the sidewalls of CNTs[20] (Figure 2h; Figure S18, Supporting Information). The L_a of TCNTs were calculated to be 3.74 nm for N,S-TCNTs-4h, 3.64 nm for N,S-TCNTs-8h, 3.65 nm for N,S-TCNTs-12h (Table S3, Supporting Information). The L_a of TCNTs is similar to that of pCNTs (L_a: 3.66 nm), which implies that the sidewalls of TCNTs may remain well undoped or slightly doped and the tips of TCNTs may be doped with heteroatoms after ball milling. In contrast, traditional N and S-doped CNTs (N,S-CNTs, see details in Figure S19, Supporting Information) obtained by annealing CNTs with thiourea, and their structures are similar to pCNTs (Figures S19a,b,S13a,b, Supporting Information). Besides, N,S-CNTs show a smaller L_a of 3.57 nm than that of pCNTs from the XRD pattern (Figure S19d, Table S3, Supporting Information), most likely due to the random doping of heteroatoms entirely on the CNTs, including sidewall. In addition, by analyzing the nitrogen adsorption–desorption isotherms of the ball-milled samples, it was found that the specific surface area and total pore volume (PV) of TCNTs are larger than those of pCNTs (Figure S20, Table S4, Supporting Information), resulting from the more opened tips of the CNTs.[21] Meanwhile, the adsorption at low relative pressure and the PV at the micropore region (<2 nm) remains identical after ball milling, indicating no micropores in the sidewalls are generated,[21a,22] which confirms that the ball milling has less damage to the sidewalls of TCNTs.

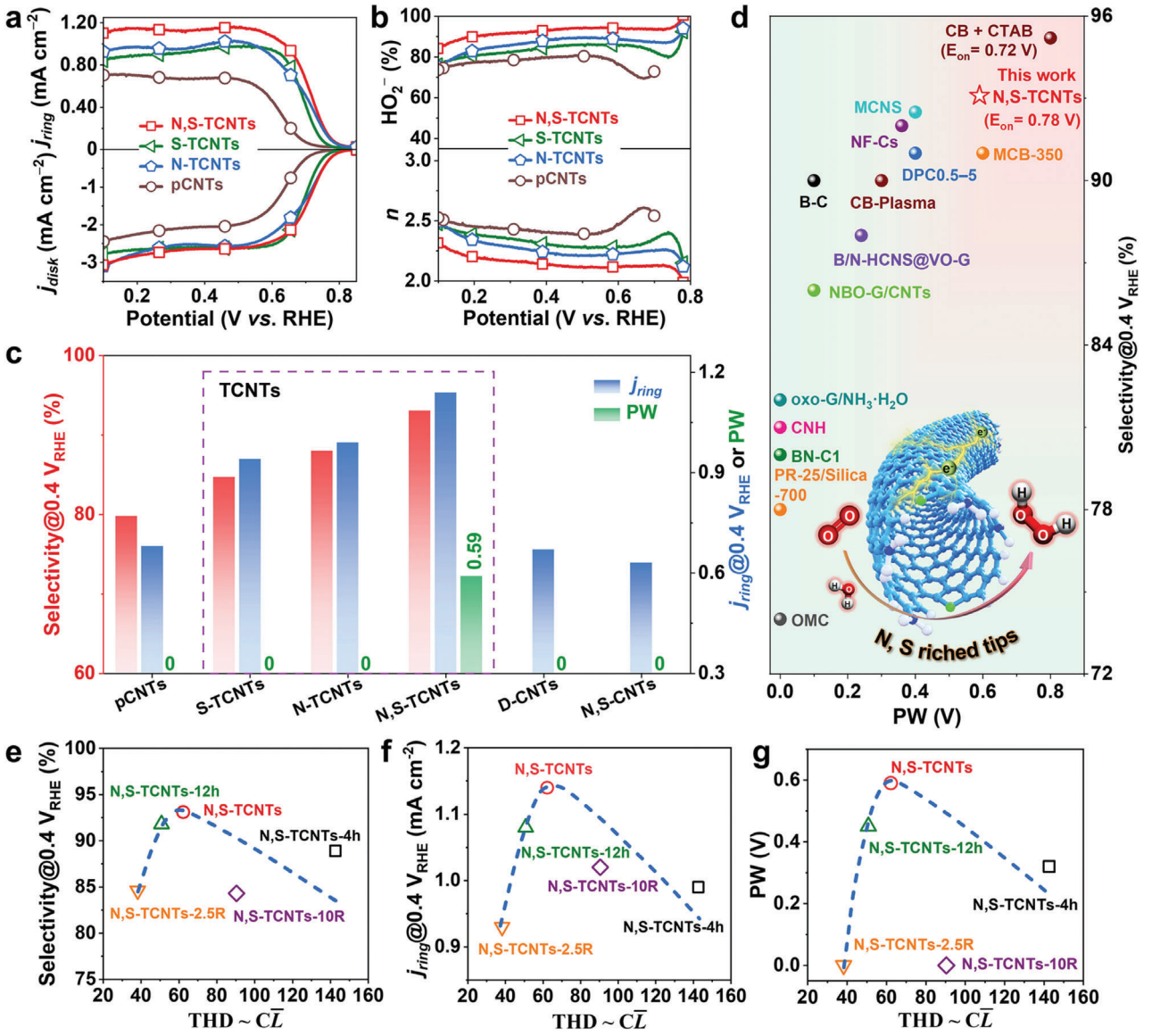

Figure 3. Electrocatalytic activities. a) The LSV curves, b) H_2O_2 selectivity and "n" of pCNTs, N-TCNTs, S-TCNTs, and N,S-TCNTs. c) Summary of j_{disk}, H_2O_2 selectivity@0.4 V, and PW. d) Comparison of H_2O_2 selectivity and PW in TNCTs with reported C-MFECs. The E_{on} of N,S-TCNTs and CB+CTAB is provided in brackets. The inset is the schematic diagram of N,S-rich CNT tips for 2e-ORR. e–g) The relationship between THD and H_2O_2 selectivity, j_{ring} (mA cm^{-2}), and PW (V) of N,S-TCNT samples.

Moreover, the linear profiles obtained from the corresponding inverse fast Fourier transformation (IFFT) images of selected areas in high-resolution TEM (HR-TEM, Figure 2i) image of typical TCNTs (N,S-TCNTs) reveal that the d-spacing of the sidewall is 0.354 nm (Figure 2j-I) corresponding to (002) facet, which is similar to that of pCNTs (d-spacing: 0.355 nm; Figure S21, Supporting Information), indicating that the sidewalls of TCNTs remain its original crystal structure. In contrast, the tip of N,S-TCNTs shows larger d-spacings of 0.372 and 0.426 nm (Figure 2j-II,III), most likely due to the expansion of carbon layers by N and/or S doping.[16a] Furthermore, the energy-dispersive X-ray spectroscopy (EDS) elemental mapping scan from high-angel annular dark-field scanning TEM (HADDF-STEM, Figure 2k-I) based on spherical aberration-corrected transmission electron microscope further confirms that the heteroatom doping, including N and S doping, is mainly concentrated at the CNT tip (but cannot completely avoid sidewall doping), although the signal of N is lower than S owing to its relatively low atomic number (Figure 2k-II). These results indicate that the heteroatoms are dominantly doped at the tips of short CNTs, which is consistent with the theoretical calculations (vide ante).

2.3. Electrocatalytic Activities of ORR to H_2O_2

To verify the effectiveness of our designed N,S-rich TCNTs, the 2e-ORR electrocatalytic activities, and selectivity were

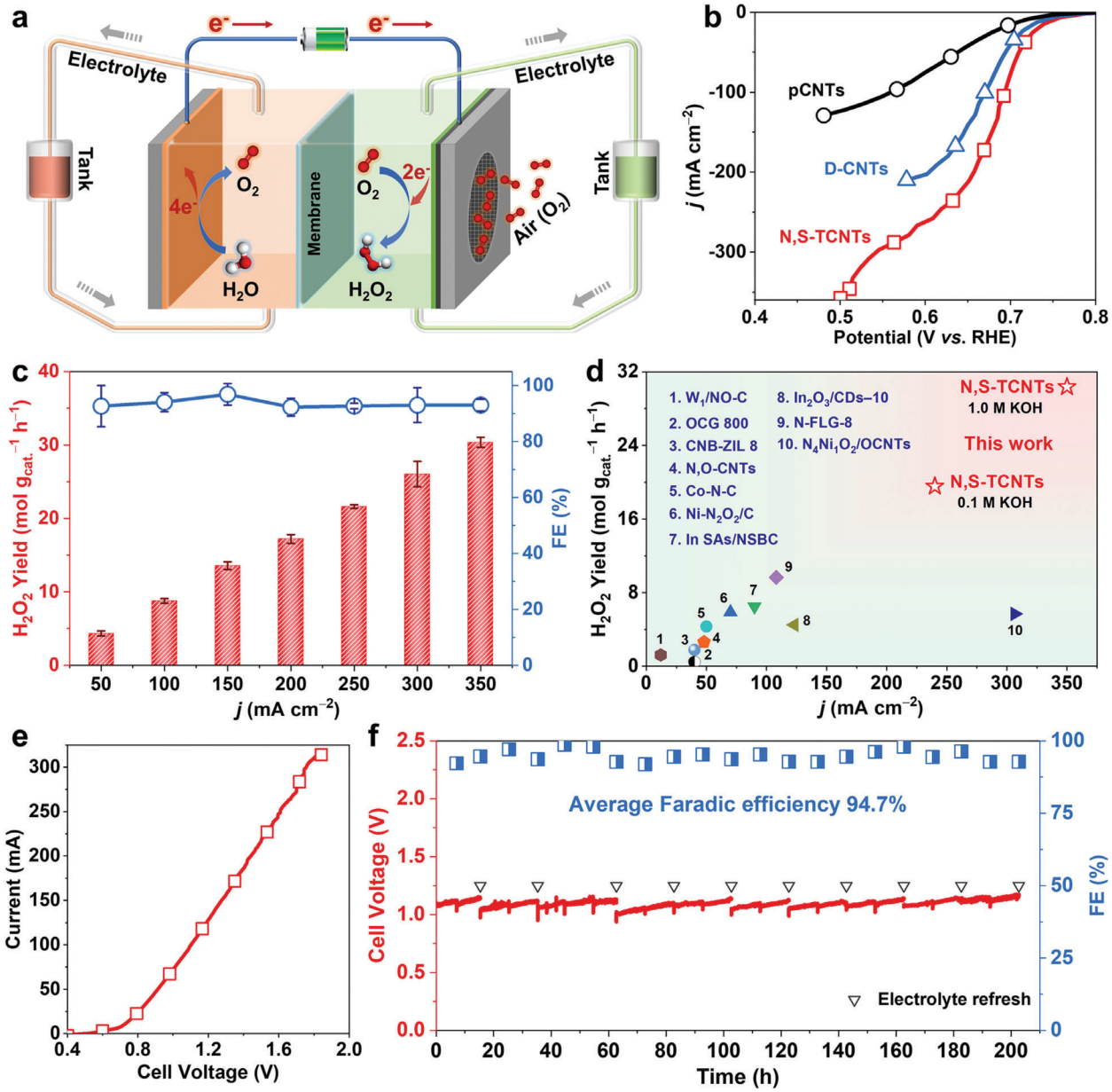

Figure 4. Flow cell based on natural air diffusion electrode. a) Schematic illustration of the FC. b) LSV curves of pCNTs, D-CNTs, and N,S-TCNTs in the 3E-FCs. c) H_2O_2 yield rate and FEs under different current densities of N,S-TCNTs in the 3E-FC. d) H_2O_2 productivity of N,S-TCNTs in comparison with that of recently reported 2e-ORR electrocatalysts. e) LSV curve and f) stability test under 100 mA of N,S-TCNTs in the 2E-FC.

evaluated on a rotating ring-disk electrode with a calibrated collection efficiency of 0.373 (Figure S22, Supporting Information). As a comparison, the N-doped and S-doped TCNTs were also prepared to reveal the vital role of heteroatom doping and the superiority of the synergistic effect of heteroatoms for electrocatalytic performance (Figures S23–S26, Supporting Information). As shown in **Figure 3**a, N,S-TCNTs exhibit a more positive onset potential (E_{on}) of 0.78 V than that of N-TCNTs (0.77 V), S-TCNTs (0.75 V), especially pCNTs (0.54 V), and even superior to most of the so-far-reported C-MFECs[1b,2c,d,4d,23] (Tables S5,S6, Supporting Information). The disk current densities (j_{disk}) of all TCNT samples are similar, but significantly higher than that of pCNTs. However, the ring current densities (j_{ring}) associated with H_2O_2 production showed significant differences. Specifically, j_{ring} follow the order: N,S-TCNTs > N-TCNTs > S-TCNTs > pCNTs. Furthermore, the calculated H_2O_2 selectivity according to the linear sweep voltammetry (LSV) curves showed that N,S-TCNTs deliver a high H_2O_2 selectivity of 93.1%@0.40 V (up to 94.5%@0.56 V), which surpasses those of pCNTs (79.8%), N-TCNTs (88.0%), and S-TCNTs (84.7%) (Figure 3b,c), and even most of the 2e-ORR based C-MFECs (Table S6, Supporting Information).[1b,2c,d,4d,23] Meanwhile, the electron transfer number ("n") of N,S-TCNTs was calculated to be 2.00–2.19 at the range

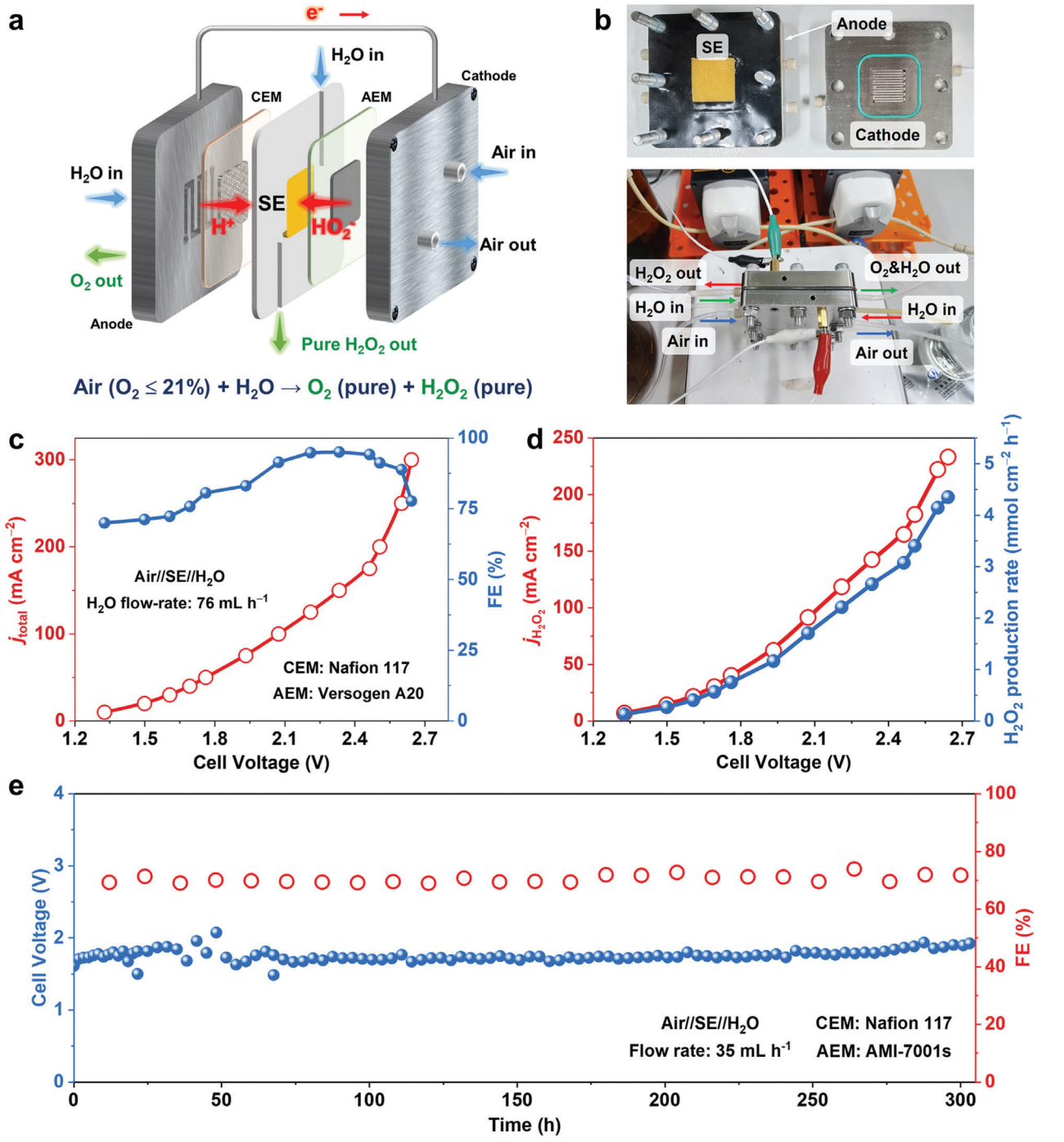

Figure 5. Solid-electrolyte cell for H_2O_2 production. a) Schematic illustration, b) digital photo of the SEC. c) j_{total}–V_{cell} curve and H_2O_2 FE, d) corresponding H_2O_2 partial currents and production rates of Air//SE//H_2O cell. e) Stability test of N,S-TCNTs at 80 mA.

of 0.78–0.20 V, which is lower than that pCNTs, N-TCNTs, and S-TCNTs (Figure 3b), indicating the favor 2e-ORR pathway on N,S-TCNTs.

During the reaction of 2e-ORR toward H_2O_2, *OOH is considered the key intermediate.[1b,c,4c,15] Since the binding energy of *OOH and *OH has a linear relationship,[24] the interaction behavior between the *OOH intermediates and the catalysts were evaluated by analyzing the adsorption behavior of *OH in the Ar-saturated electrolyte.[25] As shown in Figure S27 (Supporting Information), the lower formation potential of the OH_{ad} ($OH^- \rightarrow OH_{ad} + e^-$) indicates the stronger adsorption of *OH, which in turn means stronger adsorption of *OOH. Therefore, the adsorption strength of *OOH along the order of N-TCNTs > N,S-TCNTs > S-TCNTs > pCNTs. N-TCNTs and pCNTs

exhibit the strongest and weakest *OOH adsorption, respectively, while N,S-TCNTs own a moderate *OOH adsorption. From a theoretical point of view (Figure 1e), too strong or too weak of *OOH adsorption is not conducive to the formation of H_2O_2, and moderate adsorption provided by N, S co-doping has the opportunity to achieve high 2e-ORR activity.[1b,c,4c,15]

Moreover, the lower Tafel slope values of TCNTs (especially for N,S-TCNTs, 63.2 mV dec^{-1} and S-TCNTs, 55.5 mV dec^{-1}) than that of pCNTs (81.0 mV dec^{-1}) indicates that abundant tips with heteroatom doping play a significant role in facilitating the kinetics of 2e-ORR (Figure S28, Supporting Information). Before excluding the effect of electrochemically active surface areas (ECSA), double layer capacitance (C_{dl}) of the samples was measured by cyclic voltammetry technology (Figure S29, Supporting Information). To confirm the superior intrinsic activity of N,S-TCNTs, the turnover frequency (TOF) was estimated based on ECSA, BET (Table S4, Supporting Information), and loading mass for metal-free catalysts.[26] From Figure S30 (Supporting Information), the TOF value of N,S-TCNTs is higher than N-TCNTs and S-TCNTs, which confirms the superior intrinsic activity of N,S-TCNTs. After normalization of the kinetic current for H_2O_2 production by the C_{dl} value to obtain specific current ($j_{s,\ peroxide}$),[27] the S-TCNTs still exhibit a lower Tafel slope than pCNTs and N-TCNTs (Figure S31a, Supporting Information), suggesting that S doping is beneficial to promote the kinetics; while the $j_{s,\ peroxide}$ at 0.75 V of N-CNTs is twofold higher than those of pCNTs and S-TCNTs (Figure S31b, Supporting Information), along with large TOF value than S-TCNTs, confirming N doping could facilitate the intrinsic activity.[27]

To further investigate the importance of heteroatoms, N,S-TCNTs were annealed at 1100 °C to remove most of the N and S dopants, the resulting de-doped CNTs (D-CNTs) (see details from Figure S32, Supporting Information) show significantly lower H_2O_2 selectivity of 58.4%@0.4 V and higher Tafel slope value (63.9 mV dec^{-1}) as compared to those of N,S-TCNTs (Figure 3c; Figure S33, Supporting Information). Besides, although the sample of N,S-CNTs prepared via annealing method shows similar atomic content of N and S (1.74 at.% by XPS and 0.74 at.% by EA, Figure S19e,f, Supporting Information) compared to that of N,S-TCNTs (Tables S1,S2, Supporting Information), it also displays unsatisfactory 2e-ORR performance (Figure S33, Supporting Information, H_2O_2 selectivity: 56.4%@0.4 V, Tafel slope: 79.3 mV dec^{-1}) due to the presence of pyridinic-*N* (Figure S19e, Supporting Information), which favors the 4-electrons pathway rather than 2-electrons pathway for the ORR catalytic process.[28] Furthermore, although the value of C_{dl} for N,S-TCNTs is lower than those of N,S-CNTs (Figure S34, Supporting Information), the C_{dl}-normalized Tafel slope and H_2O_2 activities (j_s) were higher than N,S-CNTs (Figure S35, Supporting Information), further confirming their superior intrinsic activity.

The high H_2O_2 selectivity in a wide PW is beneficial for actual working conditions. Herein, the PW values (potential at H_2O_2 selectivity over 90.0% and lower than E_{on}) of prepared samples were summarized along with H_2O_2 selectivity and j_{ring}@0.4 V in Figure 3d and Table S5 (Supporting Information). TNCTs, especially N,S-TCNTs, own superior selectivity, wider PW, and higher H_2O_2 current density. Specifically, N,S-TCNTs achieved the wide PW of 0.78–0.19 V (≈0.59 V wide) for the H_2O_2 selectivity over 90.0% (Figure 3c), which overwhelms most reported C-MFECs[1b,2b,c,4c,d,23,27,29] (Figure 3d and Table S6, Supporting Information. Note: although the PW and H_2O_2 selectivity@0.4 V of N,S-TCNTs are worse than those of CB + CTAB, the E_{on} is more positive), highlighting the excellent 2e-ORR performance of N,S-TCNTs and showing potentially application in a real practical condition. Through the above analysis, the outstanding 2e-ORR performance of N,S-TCNTs may be attributed to the synergistic effect of N and S doping at the lattice tip edges (inset in Figure 3d).

In addition to the ball milling time as mentioned above, the ratio of thiourea to pCNTs (y, named as N,S-TCNTs-yR, Figures S36–S39, Supporting Information) in the precursors would also affect the length and heteroatom content of obtained N,S-TCNT samples, resulting in different catalytic properties for 2e-ORR. As shown in Figures S40,S41 (Supporting Information), the ORR performance of N,S-TCNTs-yR, including H_2O_2 selectivity, j_{ring}@0.4 V and PW, first increased and then decreased with increasing the ratio of thiourea to pCNTs (y), showing the same trend as increasing the ball milling time (Table S5, Supporting Information). As the heteroatoms were dominantly doped at the tips of TCNTs, to clarify the relationship between the 2e-ORR performance and the heteroatom contents ("C"), the tip heteroatom density (THD) in N,S-TCNT samples, proportional to "C" and $\bar{L}$ (see details from Table S7, Supporting Information), was calculated and plotted with H_2O_2 selectivity, j_{ring}, and PW (Figure 3e–g). The increase in THD benefits the 2e-ORR performance in a certain range, while the performance will decrease after a volcano peak location. From this viewpoint, a balanced THD could maximize the 2e-ORR performance, which seems to be consistent with DFT calculations showing the heteroatom distances also affect the 2e-ORR performance to somex degree.

The electrochemical impedance spectra of N,S-TCNT samples with different ball milling times and ratio of thiourea to pCNTs were also plotted (Figure S42, Supporting Information), revealing that the N,S-TCNT samples show a similar electron transfer resistance but much higher ion diffusion compared with those of pCNTs,[17] which could arise from well-retained sidewall and the abundant tips of TCNTs, respectively. In addition, the resistivity of all N,S-TCNT samples measured by the four-probe method was similar to that of pCNT (Figure S43, Supporting Information), which also could be attributed to the maximum preservation of the sidewall crystalline structure of N,S-TCNT samples. Long-term durability is another crucial parameter of electrocatalysts for practical application. After 12 h continuous testing, the j_{disk}, j_{ring}, and H_2O_2 selectivity of N,S-TCNTs show ignorable change (Figure S44, Supporting Information), indicating their relatively good durability. In addition, after the durability test, there is no significant change in the structure and composition of N,S-TCNTs (see details from Figure S45, Supporting Information).

2.4. Flow Cell Configuration Based on Natural Air Diffusion Electrode

As a result, a three-electrode flow cell (3E-FC) was fabricated to further evaluate 2e-ORR performance using natural air as the O_2 source (**Figure 4**a), rather than pure O_2 usually used in previous

literature.[2a,14a,15,30] LSV curves show that the FC with N,S-TCNTs deliver a current density of 216.7 mA cm^{-2}@0.65 V (Figure 4b), which is much higher than these based on pCNTs (42.0 mA cm^{-2}) and D-CNTs (141.0 mA cm^{-2}).

Additionally, the FEs of 2e-ORR and the H_2O_2 yield under different current densities (Figure 4c) were quantified by cerium sulfate titration method (Supporting Information) via UV/Vis spectrophotometry[14a] (see details from Figure S46, Supporting Information). The H_2O_2 FE of the FC based on N,S-TCNTs remains over 90.0% at a current density range from 50 to 350 mA cm^{-2} (Tables S8–S10, Supporting Information), achieving the highest H_2O_2 yield rate of 30.37 mol $g_{cat.}^{-1}$ h^{-1} at 350 mA cm^{-2} in 1.0 M KOH electrolyte (19.56 mol $g_{cat.}^{-1}$ h^{-1}@240 mA cm^{-2} in 0.1 M KOH electrolyte, Figure S47, Supporting Information), which outperforms that of almost reported electrocatalysts (Figure 4d, Table S11, Supporting Information).[1b,2a,4a,c,14a,15,30,31] Thus, N,S-TCNTs exhibit a great potential to deliver industrial-level electrocatalytic current density with high H_2O_2 selectivity.

2E-FC was also employed to evaluate the 2e-ORR performance of N,S-TCNTs, as it makes a step closer to the practical application when compared with 3E-FC.[32] The overall cell current increases rapidly along with the increased V_{cell}, reaching a high current of 300 mA at a relatively low V_{cell} of 1.76 V (Figure 4e). Note that N,S-TCNTs can undergo at least a 200-h stability test, but not limited to, with negligible V_{cell} increment at 100 mA current (Figure 4f). Specifically, the V_{cell} and FE remained stable at ≈1.09 V and 94.7% during the process, making the designed TCNTs in this work good candidates for on-site H_2O_2 synthesis.

2.5. Pure H_2O_2 Synthesis via Solid-Electrolyte Cells

To avoid the high-cost and complicated post-treatment processes required to purify H_2O_2 solution in the traditional configurations including 3E-FC and 2E-FC, an air-based SEC (Air//SE//H_2O) was assembled to synthesize pure H_2O_2 solution (**Figure 5**a,b, see details from Figure S48, Supporting Information). The cathode side was supplied with air flow, while the anode side was supplied with deionized H_2O. Using N,S-TCNTs as cathode catalysts, high FE (up to 95.1%@150 mA cm^{-2}) can be reached within a wide E_{cell} and total current density (j_{total}) as high as 300 mA cm^{-2} (Figure 5c). Meanwhile, the highest production rate of 4.35 mmol cm^{-2} h^{-1} can be achieved at 300 mA cm^{-2} with an H_2O_2 partial current density of ≈233.2 mA cm^{-2} (Figure 5d), which is superior to that of almost reported SECs with C-MFECs using air as O_2 source.[1a,33] N,S-TCNTs can undergo over 300 h stability tests for a continuous pure H_2O_2 solution synthesis (1022 ppm) without V_{cell} significant degradation at a fixed current of 80 mA (Figure 5e). Besides, the FE remained stable at ≈70% for the entire test, which also shows excellent stable production of pure H_2O_2 solution in SEC.

3. Conclusion

In summary, we have demonstrated that engineering the cleavage of CNTs can effectively modulate their tip atomic environment for superior 2e-ORR catalytic performance. MD simulations and experimental results revealed that ball-milling could lead to the formation of TCNTs with unique heteroatoms doped on zigzag edges. It was found that the combination of amino-*N* and thiophene-*S* exhibits more optimal ΔG_{*OOH}, thus presenting exceptional high activity with remarkable H_2O_2 selectivity in a broad PW (over 90.0% from 0.19 to 0.78 V). Additionally, using natural air as an O_2 source, N,S-TCNTs achieved superior H_2O_2 productivity and stability in both flow cell and solid-electrolyte configuration, demonstrating its great prospect for advanced technological applications. The strategy presented herein provides an ideal scenario to develop highly selective ORR C-MFECs by accurately designing a specific atomic environment for H_2O_2 electrochemical synthesis and beyond.

Supporting Information

Supporting Information is available from the Wiley Online Library or from the author.

Acknowledgements

This work was partly financially supported by the National Natural Science Foundation of China (52172179), the Fundamental Research Funds for the Central Universities (buctrc202118), an open fund of the Key Lab of Organic Optoelectronics and Molecular Engineering of Ministry of Education (No. 53223000122), National Natural Science Foundation of China (Grant Nos. 11972349, 11790292), and the Strategic Priority Research Program of the Chinese Academy of Sciences (Grant No. XDB22040503).

Conflict of Interest

The authors declare no conflict of interest.

Data Availability Statement

The data that support the findings of this study are available from the corresponding author upon reasonable request.

Keywords

carbon nanotubes, electrocatalysis, hydrogen peroxide, pure H_2O_2 solution production, tip atomic environment

Received: April 26, 2023
Revised: July 1, 2023
Published online: August 3, 2023

[1] a) C. Xia, Y. Xia, P. Zhu, L. Fan, H. Wang, *Science* **2019**, *366*, 226; b) Y. Xia, X. Zhao, C. Xia, Z.-Y. Wu, P. Zhu, J. Y. Kim, X. Bai, G. Gao, Y. Hu, J. Zhong, Y. Liu, H. Wang, *Nat. Commun.* **2021**, *12*, 4225; c) Z. Lu, G. Chen, S. Siahrostami, Z. Chen, K. Liu, J. Xie, L. Liao, T. Wu, D. Lin, Y. Liu, T. F. Jaramillo, J. K. Nørskov, Y. Cui, *Nat. Catal.* **2018**, *1*, 156; d) S. Ye, C. Ding, M. Liu, A. Wang, Q. Huang, C. Li, *Adv. Mater.* **2019**, *31*, 1902069; e) S. C. Perry, D. Pangotra, L. Vieira, L.-I. Csepei, V. Sieber, L. Wang, C. Ponce de León, F. C. Walsh, *Nat. Rev. Chem.* **2019**, *3*, 442.

[2] a) Z. Tian, Q. Zhang, L. Thomsen, N. Gao, J. Pan, R. Daiyan, J. Yun, J. Brandt, N. López-Salas, F. Lai, Q. Li, T. Liu, R. Amal, X. Lu, M.

Antonietti, *Angew. Chem., Int. Ed.* **2022**, *61*, e202206915; b) F. Xiang, X. Zhao, J. Yang, N. Li, W. Gong, Y. Liu, A. Burguete-Lopez, Y. Li, X. Niu, A. Fratalocchi, *Adv. Mater.* **2023**, *35*, 2208533; c) Z. Wang, Q.-K. Li, C. Zhang, Z. Cheng, W. Chen, E. A. McHugh, R. A. Carter, B. I. Yakobson, J. M. Tour, *ACS Catal.* **2021**, *11*, 2454; d) L. Han, Y. Sun, S. Li, C. Cheng, C. E. Halbig, P. Feicht, J. L. Hübner, P. Strasser, S. Eigler, *ACS Catal.* **2019**, *9*, 1283.

[3] a) H. W. Kim, M. B. Ross, N. Kornienko, L. Zhang, J. Guo, P. Yang, B. D. McCloskey, *Nat. Catal.* **2018**, *1*, 282; b) G.-F. Han, F. Li, W. Zou, M. Karamad, J.-P. Jeon, S.-W. Kim, S.-J. Kim, Y. Bu, Z. Fu, Y. Lu, S. Siahrostami, J.-B. Baek, *Nat. Commun.* **2020**, *11*, 2209; c) J. Liu, N. P. Wickramaratne, S. Z. Qiao, M. Jaroniec, *Nat. Mater.* **2015**, *14*, 763.

[4] a) S. Xu, R. Lu, K. Sun, J. Tang, Y. Cen, L. Luo, Z. Wang, S. Tian, X. Sun, *Adv. Sci.* **2022**, *9*, 2201421; b) H. Zhao, X. Shen, Y. Chen, S.-N. Zhang, P. Gao, X. Zhen, X.-H. Li, G. Zhao, *Chem. Commun.* **2019**, *55*, 6173; c) M. Fan, Z. Wang, K. Sun, A. Wang, Y. Zhao, Q. Yuan, R. Wang, J. Raj, J. Wu, J. Jiang, L. Wang, *Adv. Mater.* **2023**, *35*, 2209086; d) N. Jia, T. Yang, S. Shi, X. Chen, Z. An, Y. Chen, S. Yin, P. Chen, *ACS Sustainable Chem. Eng.* **2020**, *8*, 2883.

[5] I. Mazov, V. L. Kuznetsov, I. A. Simonova, A. I. Stadnichenko, A. V. Ishchenko, A. I. Romanenko, E. N. Tkachev, O. B. Anikeeva, *Appl. Surf. Sci.* **2012**, *258*, 6272.

[6] a) W. Yuan, Y. Zhou, Y. Li, C. Li, H. Peng, J. Zhang, Z. Liu, L. Dai, G. Shi, *Sci. Rep.* **2013**, *3*, 2248; b) D.-e. Jiang, B. G. Sumpter, S. Dai, *J. Chem. Phys.* **2007**, *126*, 134701; c) D. Deng, L. Yu, X. Pan, S. Wang, X. Chen, P. Hu, L. Sun, X. Bao, *Chem. Commun.* **2011**, *47*, 10016; d) A. Shen, Y. Zou, Q. Wang, R. A. Dryfe, X. Huang, S. Dou, L. Dai, S. Wang, *Angew. Chem., Int. Ed.* **2014**, *53*, 10804.

[7] I.-Y. Jeon, H.-J. Choi, M. J. Ju, I. T. Choi, K. Lim, J. Ko, H. K. Kim, J. C. Kim, J.-J. Lee, D. Shin, S.-M. Jung, J.-M. Seo, M.-J. Kim, N. Park, L. Dai, J.-B. Baek, *Sci. Rep.* **2013**, *3*, 2260.

[8] I.-Y. Jeon, H.-J. Choi, S.-M. Jung, J.-M. Seo, M.-J. Kim, L. Dai, J.-B. Baek, *J. Am. Chem. Soc.* **2013**, *135*, 1386.

[9] J. Xu, I. Y. Jeon, J. M. Seo, S. Dou, L. Dai, J. B. Baek, *Adv. Mater.* **2014**, *26*, 7317.

[10] X. Fan, D. W. Chang, X. Chen, J.-B. Baek, L. Dai, *Curr. Opin. Chem. Eng.* **2016**, *11*, 52.

[11] a) L. Dai, Y. Xue, L. Qu, H.-J. Choi, J.-B. Baek, *Chem. Rev.* **2015**, *115*, 4823; b) B. Q. Wei, R. Vajtai, P. M. Ajayan, *Appl. Phys. Lett.* **2001**, *79*, 1172; c) K. Jiang, S. Back, A. J. Akey, C. Xia, Y. Hu, W. Liang, D. Schaak, E. Stavitski, J. K. Nørskov, S. Siahrostami, H. Wang, *Nat. Commun.* **2019**, *10*, 3997.

[12] a) Á. Kukovecz, T. Kanyó, Z. Kónya, I. Kiricsi, *Carbon* **2005**, *43*, 994; b) N. Pierard, A. Fonseca, Z. Konya, I. Willems, G. Van Tendeloo, J. B. Nagy, *Chem. Phys. Lett.* **2001**, *335*, 1.

[13] J. Huang, S.-C. Her, X. Yang, M. Zhi, *Nanomaterials* **2018**, *8*, 786.

[14] a) L. Li, C. Tang, Y. Zheng, B. Xia, X. Zhou, H. Xu, S.-Z. Qiao, *Adv. Energy Mater.* **2020**, *10*, 2000789; b) K. H. Koh, Y. J. Kim, A. H. B. Mostaghim, S. Siahrostami, T. H. Han, Z. Chen, *ACS Mater. Lett.* **2022**, *4*, 320; c) O. L. Li, Y. Wada, A. Kaneko, H. Lee, T. Ishizaki, *ChemElectroChem* **2018**, *5*, 1995; d) X. Xiao, T. Wang, J. Bai, F. Li, T. Ma, Y. Chen, *ACS Appl. Mater. Interfaces* **2018**, *10*, 42534; e) E. Mitraka, M. Gryszel, M. Vagin, M. J. Jafari, A. Singh, M. Warczak, M. Mitrakas, M. Berggren, T. Ederth, I. Zozoulenko, X. Crispin, E. D. Głowacki, *Adv. Sustainable Syst.* **2019**, *3*, 1800110; f) R. Hu, Y. Cui, B. Huang, L. Guan, *ACS Appl. Mater. Interfaces* **2021**, *13*, 35856.

[15] E. Zhang, L. Tao, J. An, J. Zhang, L. Meng, X. Zheng, Y. Wang, N. Li, S. Du, J. Zhang, D. Wang, Y. Li, *Angew. Chem., Int. Ed.* **2022**, *61*, e202117347.

[16] a) I. Y. Jeon, S. Zhang, L. Zhang, H. J. Choi, J. M. Seo, Z. Xia, L. Dai, J. B. Baek, *Adv. Mater.* **2013**, *25*, 6138; b) M.-J. Kim, I.-Y. Jeon, J.-M. Seo, L. Dai, J.-B. Baek, *ACS Nano* **2014**, *8*, 2820.

[17] Y. Long, F. Ye, L. Shi, X. Lin, R. Paul, D. Liu, C. Hu, *Carbon* **2021**, *179*, 365.

[18] S. Yang, L. Zhi, K. Tang, X. Feng, J. Maier, K. Müllen, *Adv. Funct. Mater.* **2012**, *22*, 3634.

[19] a) K. Sadowska, K. P. Roberts, R. Wiser, J. F. Biernat, E. Jabłonowska, R. Bilewicz, *Carbon* **2009**, *47*, 1501; b) S. Osswald, M. Havel, Y. Gogotsi, *J. Raman Spectrosc.* **2007**, *38*, 728.

[20] Shilpa, S. K. D., M. A. F. Afzal, S. Srivastava, S. Patil, A. Sharma, *Carbon* **2016**, *108*, 135.

[21] a) S. Delpeux, K. Szostak, E. Frackowiak, F. Béguin, *Chem. Phys. Lett.* **2005**, *404*, 374; b) E. Raymundo-Pinero, D. Cazorla-Amorós, A. Linares-Solano, S. Delpeux, E. Frackowiak, K. Szostak, F. Béguin, *Carbon* **2002**, *40*, 1614.

[22] Y. Chen, C. Liu, F. Li, H.-M. Cheng, *J. Porous Mater.* **2006**, *13*, 141.

[23] a) P. Chakthranont, S. Nitrathorn, S. Thongratkaew, P. Khemthong, H. Nakajima, R. Supruangnet, T. Butburee, N. Sano, K. Faungnawakij, *ACS Appl. Energy Mater.* **2021**, *4*, 12436; b) K. Wang, Q. Dai, C. Hu, Y. Tong, Y. Wang, S. Song, L. Dai, *Chem. Eng. J.* **2021**, *416*, 128338; c) Y. Wu, Z. Gao, Y. Feng, Q. Cui, C. Du, C. Yu, L. Liang, W. Zhao, J. Feng, J. Sun, R. Yang, J. Sun, *Appl. Catal., B* **2021**, *298*, 120572; d) S. Chen, Z. Chen, S. Siahrostami, D. Higgins, D. Nordlund, D. Sokaras, T. R. Kim, Y. Liu, X. Yan, E. Nilsson, R. Sinclair, J. K. Nørskov, T. F. Jaramillo, Z. Bao, *J. Am. Chem. Soc.* **2018**, *140*, 7851; e) A. Yu, G. Ma, L. Zhu, R. Zhang, Y. Li, S. Yang, H.-Y. Hsu, P. Peng, F.-F. Li, *Appl. Catal., B* **2022**, *307*, 121161; f) B. Huang, Y. Cui, R. Hu, J. Huang, L. Guan, *ACS Appl. Energy Mater.* **2021**, *4*, 4620.

[24] A. Kulkarni, S. Siahrostami, A. Patel, J. K. Nørskov, *Chem. Rev.* **2018**, *118*, 2302.

[25] a) D. Strmcnik, K. Kodama, D. van der Vliet, J. Greeley, V. R. Stamenkovic, N. M. Marković, *Nat. Chem.* **2009**, *1*, 466; b) R. Subbaraman, D. Tripkovic, K.-C. Chang, D. Strmcnik, A. P. Paulikas, P. Hirunsit, M. Chan, J. Greeley, V. Stamenkovic, N. M. Markovic, *Nat. Mater.* **2012**, *11*, 550.

[26] J.-C. Li, X. Qin, P.-X. Hou, M. Cheng, C. Shi, C. Liu, H.-M. Cheng, M. Shao, *Carbon* **2019**, *147*, 303.

[27] K.-H. Wu, D. Wang, X. Lu, X. Zhang, Z. Xie, Y. Liu, B.-J. Su, J.-M. Chen, D.-S. Su, W. Qi, S. Guo, *Chem* **2020**, *6*, 1443.

[28] D. Guo, R. Shibuya, C. Akiba, S. Saji, T. Kondo, J. Nakamura, *Science* **2016**, *351*, 361.

[29] a) Q. Tian, L. Jing, Y. Chen, P. Su, C. Tang, G. Wang, J. Liu, *Sustainable Mater. Technol.* **2022**, *32*, e00398; b) L. Jing, C. Tang, Q. Tian, T. Liu, S. Ye, P. Su, Y. Zheng, J. Liu, *ACS Appl. Mater. Interfaces* **2021**, *13*, 39763.

[30] a) C. Xiao, L. Cheng, Y. Zhu, G. Wang, L. Chen, Y. Wang, R. Chen, Y. Li, C. Li, *Angew. Chem., Int. Ed.* **2022**, *61*, e202206544; b) F. Zhang, Y. Zhu, C. Tang, Y. Chen, B. Qian, Z. Hu, Y.-C. Chang, C.-W. Pao, Q. Lin, S. A. Kazemi, Y. Wang, L. Zhang, X. Zhang, H. Wang, *Adv. Funct. Mater.* **2022**, *32*, 2110224; c) J. Wu, Y. Han, Y. Bai, X. Wang, Y. Zhou, W. Zhu, T. He, Y. Wang, H. Huang, Y. Liu, Z. Kang, *Adv. Funct. Mater.* **2022**, *32*, 2203647; d) K. Lee, J. Lim, M. J. Lee, K. Ryu, H. Lee, J. Y. Kim, H. Ju, H.-S. Cho, B.-H. Kim, M. C. Hatzell, J. Kang, S. W. Lee, *Energy Environ. Sci.* **2022**, *15*, 2858; e) Y. Sun, L. Silvioli, N. R. Sahraie, W. Ju, J. Li, A. Zitolo, S. Li, A. Bagger, L. Arnarson, X. Wang, T. Moeller, D. Bernsmeier, J. Rossmeisl, F. Jaouen, P. Strasser, *J. Am. Chem. Soc.* **2019**, *141*, 12372.

[31] a) Y. Wang, R. Shi, L. Shang, G. I. N. Waterhouse, J. Zhao, Q. Zhang, L. Gu, T. Zhang, *Angew. Chem., Int. Ed.* **2020**, *59*, 13057; b) Q. Yuan, M. Fan, Y. Zhao, J. Wu, J. Raj, Z. Wang, A. Wang, H. Sun, X. Xu, Y. Wu, K. Sun, J. Jiang, *Appl. Catal., B* **2023**, *324*, 122195.

[32] E. Jung, H. Shin, W. Hooch Antink, Y.-E. Sung, T. Hyeon, *ACS Energy Lett.* **2020**, *5*, 1881.

[33] Y. Zhao, N. Deng, Z. Fan, Z.-T. Hu, L. Fan, J. Zhou, X. Huang, *Chem. Eng. J.* **2022**, *430*, 132829.